

Second-harmonic generation of structured light by transition-metal dichalcogenide metasurfacesLing Ling Meng ¹, Xiaoyan Y. Z. Xiong,² Tian Xia,¹ Qin S. Liu,² Li Jun Jiang,² Wei E. I. Sha ^{3,*} and Weng Cho Chew ^{4,†}¹*Department of Electrical and Computer Engineering, University of Illinois at Urbana-Champaign, Illinois 61820, USA*²*Department of Electrical and Electronic Engineering, University of Hong Kong, Hong Kong, China*³*Key Laboratory of Micro-Nano Electronic Devices and Smart Systems of Zhejiang Province, College of Information Science and Electronic Engineering, Zhejiang University, Hangzhou 310027, China*⁴*School of Electrical and Computer Engineering, Purdue University, Indiana 47907, USA*

(Received 7 May 2020; accepted 8 September 2020; published 12 October 2020)

Structured light characterized by spatially inhomogeneous optical fields found rich applications in optical communication, sensing, microscopy, manipulation, and quantum information. While generation of structured light has been extensively studied in linear optics, the nonlinear optical process, particularly in two-dimensional (2D) materials, is an emerging alternative for generating structured light at shorter wavelengths. In this work, we theoretically demonstrate that radially and azimuthally polarized beams and vortex beams carrying orbital angular momentum could be generated at second-harmonic frequencies by using 2D material-based metasurfaces comprising the same transition-metal dichalcogenide meta-atoms. Manipulation of translations and orientations of anisotropically nonlinear meta-atoms exhibiting a threefold rotation-symmetrical crystalline structure induces strong nonlinear spin-orbital coupling, which enables simultaneous control of spatial phase and polarization in second-harmonic generation. The nonlinear transition-metal dichalcogenide metasurface proposed is promising for on-chip integration of nonlinear generation of structured light.

DOI: [10.1103/PhysRevA.102.043508](https://doi.org/10.1103/PhysRevA.102.043508)**I. INTRODUCTION**

It is well known that plane waves have independent degrees of freedom, including frequency, amplitude, polarization, and phase. Fundamentally different from plane waves, structured light has inhomogeneous and correlated amplitude, polarization, and phase. As additional degrees of freedom, the spatially inhomogeneous fields occur at the subwavelength scales of nano-optics due to the strong spin-orbital coupling when polarized photons interact with inhomogeneous media [1]. Structured light, including Hermite-Gaussian and Bessel beams [2,3], Laguerre-Gaussian beams [3,4] with helical phase front carrying orbital angular momentum (OAM), and radially and azimuthally polarized vector beams [5,6], brings novel functions to optical nanodevices and advances important applications in optical and quantum manipulation, microscopy, imaging, sensing, and communications [7]. For example, the radial polarized beam has been applied to high-resolution imaging attributed to its tighter focusing spot [8]. It can also be used in trapping nanoparticles since the beam exerts a larger longitudinal force on the particles [9]. Moreover, single-molecule localization microscopy [10] and a particle exchanger [11] employ the azimuthal polarized beam. Additionally, recent studies show potential applications of structured light in optical communications to gain communication channels through “mode-division multiplexing” [12,13].

One of tools to generate structured light is based on bulk materials and volumetric structures [14–18]. However, the diffraction effect often makes on-chip integration of these bulk devices impossible. Alternatively, a metasurface [19–21] that is a planar structure locally modifying the spatial pattern of light in reflection or transmission offers inspiring solutions to tackle the problem. It not only opens new paradigms for generating structured light at fundamental and high harmonics [22–24] but also deepens the physical understanding of linear and nonlinear spin-orbit interaction of light at subwavelength scales [25–34]. Metasurfaces based on van der Waals materials have been reported for controlling light in linear optics [35,36]. Most previous works on nonlinear generation of structured light are based on geometric configuration of the meta-atoms (like split resonant rings, U-shaped resonators, etc.). Very recently, the nonlinear generation of structured light by two-dimensional (2D) materials and plasmonic nanostructure hybridized metasurfaces were reported in [37,38].

In this work, we propose a 2D material-based metasurface platform to generate structured light at second harmonics. The meta-atoms of the metasurface are the transition-metal dichalcogenide (TMDC) flakes exhibiting anisotropic second-order susceptibility and threefold rotation-symmetrical crystalline structure. The TMDC monolayer has strong second-harmonic generation (SHG) due to the absence of inversion symmetry. The WS_2 adopted in this work has a magnitude of the effective bulk quadratic nonlinear susceptibility comparable to that of GaAs (a medium with strong bulk SHG) in the visible regime [39]. Using identical meta-atoms with tailored translations and orientations,

*weisha@zju.edu.cn

†wcchew@purdue.edu

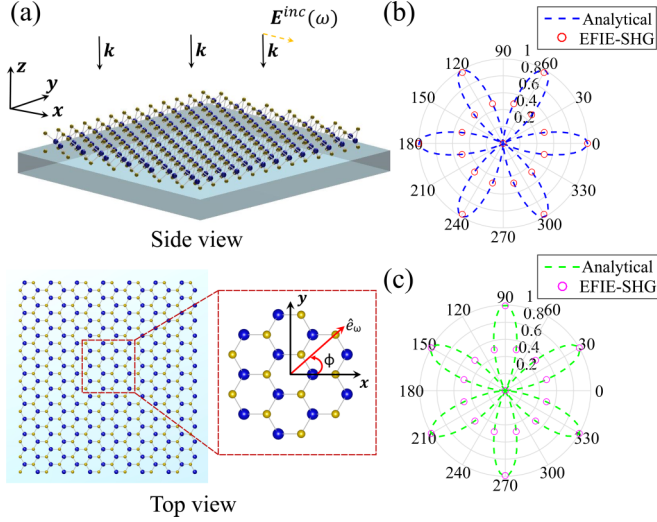


FIG. 1. (a) Side and top views of the TMDC monolayer at the xy plane. The incident plane wave propagates along the $-z$ direction. The polarization angle with respect to the armchair direction (i.e., the x axis) is denoted as ϕ . (b) Polar plot for the second-harmonic intensity of the parallel component. (c) Polar plot for the second-harmonic intensity of the perpendicular component. In (b) and (c), the EFIE-SHG results (second-harmonic generation by the electrical field integral equation) agree well with the analytical solutions: $I_{\parallel,2\omega} \propto \cos^2(3\phi)$ and $I_{\perp,2\omega} \propto \sin^2(3\phi)$. The threefold rotation-symmetrical crystalline structure generates a characteristic sixfold polar pattern for the second-harmonic intensities.

the metasurfaces could generate radially and azimuthally polarized beams and vortex beams carrying OAM at second-harmonic frequencies. Different from [37,38], we make use of all-TMDC flakes to generate various structured light, which allows for ultrathin metasurface designs. This merit can satisfy the requirements for ultracompact sources of structured light in many evolutionary applications [13]. In addition, the TMDC-based metasurface is compatible with a complementary-metal-oxide-semiconductor fabrication process [40,41]. Therefore, the metasurface composed of TMDC flakes may become a competitive platform for generation of structured light at second harmonics.

II. THEORY AND DISCUSSION

A. Second-harmonic generation of the TMDC monolayer

The 2D TMDCs are semiconducting materials, which renders them particularly suitable to be employed in nanoscale light management in optical and optoelectronic devices. They have noncentrosymmetric atomic lattices and thus allow even-order nonlinear optical processes. The crystalline structures of the TMDC with an odd number of layers belong to the D_{3h} space group, showing the threefold rotational symmetry and quadratically nonlinear susceptibility tensor with a single nonzero element [39,42,43]:

$$\chi^{(2)} \equiv \chi_{xxx}^{(2)} = -\chi_{xyy}^{(2)} = -\chi_{yyx}^{(2)} = -\chi_{yxy}^{(2)}, \quad (1)$$

where x is the armchair direction and y is the zigzag direction [see the inset in Fig. 1(a), top view]. It was experimentally reported that the TMDC monolayer has the maximum strength

of SHG at normal incidence [43]; therefore, the design in this work will focus only on the monolayer structure.

Figure 1(a) presents the configuration of the TMDC monolayer flattened on a transparent and thin substrate (aluminum oxide or silicon oxide film), illuminated by a normal-incidence wave propagating along the $-z$ direction. If the wave has a linear polarization vector \hat{e}_ω , then the generated second-harmonic wave $\mathbf{E}(2\omega)$ polarized at a given direction $\hat{e}_{2\omega}$ can be expressed as

$$\mathbf{E}(2\omega) \cdot \hat{e}_{2\omega} = C \hat{e}_{2\omega} \cdot \chi^{(2)} : \hat{e}_\omega \hat{e}_\omega, \quad (2)$$

where ω is the fundamental frequency, 2ω is the second-harmonic frequency, and C is a certain constant related to the local-field factors determined by the local medium. If the analyzer ($\hat{e}_{2\omega}$) points to the direction of fundamental polarization, the component parallel to the analyzer of the generated second-harmonic electric field (\mathbf{E} field) can be expressed as (provided in Appendix A)

$$E_{\parallel}(2\omega) = C \chi^{(2)} \cos(3\phi), \quad (3)$$

where ϕ is the angle between the incident wave polarization and the x axis (the armchair direction is aligned with the x axis). The number 3 is a critical characterizer for the anisotropic nonlinear susceptibility with threefold rotational symmetry. Similarly, the component perpendicular to the analyzer can be derived as

$$E_{\perp}(2\omega) = -C \chi^{(2)} \sin(3\phi). \quad (4)$$

Note that, the right-hand rule is applied throughout. The above perpendicular component satisfies $\hat{E}_{\parallel} \times \hat{E}_{\perp} = \hat{z}$.

B. Electric-field integral equation for TMDC monolayers

We use the electrical-field integral equation (EFIE) with the impedance boundary condition to calculate the surface current on the TMDC monolayer at the fundamental frequency [44,45]. In our theoretical model, it is reasonable to ignore substrate effects because its relative permittivity is small enough that it does not affect the polarization of the induced surface current at fundamental frequency, and the nonlinear response from the substrate is sufficiently weak compared to the TMDC monolayer in the visible regime [46] (e.g., hexagonal boron nitride, which is usually used as the substrate in experiments). The integral equation can be expressed as

$$\mathcal{L}_\omega(\mathbf{r}, \mathbf{r}') \cdot \mathbf{J}_{s,\omega}(\mathbf{r}') - \frac{1}{\sigma_s} \{\mathbf{J}_{s,\omega}(\mathbf{r})\} = -\mathbf{E}^{\text{inc}}(\mathbf{r}), \quad (5)$$

where integration is implied over repeated variables. Here $\mathbf{J}_{s,\omega}$ is the surface electric current, σ_s is the surface conductivity at the fundamental frequency, and \mathbf{E}^{inc} is the incident electric field. More explicitly, the operator \mathcal{L} represents

$$\mathcal{L}_\omega(\mathbf{r}, \mathbf{r}') = i\omega\mu \int_S \left(\bar{\mathbf{I}} + \frac{\nabla\nabla}{k^2} \right) \frac{e^{ik|\mathbf{r}-\mathbf{r}'|}}{4\pi|\mathbf{r}-\mathbf{r}'|}, \quad (6)$$

where $\bar{\mathbf{I}}$ is the identity matrix, μ is the permeability of air, k is the wave number in air at the fundamental frequency, and S is the surface of the monolayer.

After a geometrical discretization of the TMDC flake with triangular patches, the surface current can be expanded with Rao-Wilton-Glisson (RWG) basis functions (two adjacent triangles straddled as one edge basis function). Let $\{\Lambda_n(\mathbf{r})\}$ be a RWG basis function, so that the surface current $\mathbf{J}_{s,\omega}(\mathbf{r})$ can be written as $\mathbf{J}_{s,\omega}(\mathbf{r}) = \sum_n J_{\omega,n} \Lambda_n(\mathbf{r})$ for N coefficients $\{J_{\omega,n}\}$. Testing the integral equation with the same basis functions (Galerkin's method), Eq. (5) can be converted into a representation of the matrix-vector product:

$$\left[\bar{\mathbf{L}}_\omega - \frac{1}{\sigma_s} \bar{\mathbf{G}} \right] \cdot \mathbf{J}_\omega = \mathbf{g}, \quad (7)$$

where

$$[\bar{\mathbf{L}}_\omega]_{mn} = \langle \Lambda_m(\mathbf{r}), \mathcal{L}_\omega(\mathbf{r}, \mathbf{r}') \Lambda_n(\mathbf{r}') \rangle, \quad (8)$$

$$[\bar{\mathbf{G}}]_{mn} = \langle \Lambda_m(\mathbf{r}), \Lambda_n(\mathbf{r}') \rangle, \quad (9)$$

$$[\mathbf{J}_\omega]_n = J_{\omega,n}, \quad [\mathbf{g}]_n = \langle \Lambda_m(\mathbf{r}), -\mathbf{E}^{\text{inc}}(\mathbf{r}) \rangle. \quad (10)$$

Here, $\langle \cdot, \cdot \rangle$ denotes the unconjugated inner product $\langle f, g \rangle = \int f(\mathbf{r})g(\mathbf{r})d\mathbf{r}$, and $\bar{\mathbf{G}}$ is also called the Gram matrix for the RWG basis.

For the convenience of numerical computation, the E field at fundamental frequency $\mathbf{E}(\omega)$ is calculated at the center of each triangular patch. Then the surface currents at second-harmonic frequency is calculated by

$$\mathbf{J}_{s,2\omega} \cdot \hat{\mathbf{e}}_{2\omega} = \hat{\mathbf{e}}_{2\omega} \cdot \sigma_s^{(2)} : \mathbf{E}(\omega) \mathbf{E}(\omega). \quad (11)$$

The $\sigma_s^{(2)}$ is the component of second-harmonic surface conductivity tensor:

$$\sigma_s^{(2)} = -i\epsilon_0(2\omega)\chi^{(2)}, \quad (12)$$

where $\chi^{(2)}$ is the second-harmonic susceptibility in Eq. (1). The scattered electric field at second harmonics is calculated by

$$\mathbf{E}^{\text{sca}}(2\omega) = \mathcal{L}_{2\omega}\{\mathbf{J}_{s,2\omega}\}. \quad (13)$$

Note that $\mathbf{J}_{s,2\omega}$ is discretized on each triangular patch numerically, while $\mathcal{L}_{2\omega}$ is established on the edge basis of RWG. Therefore, the Gram matrix $\bar{\mathbf{G}}$ in (9) is applied to convert $\mathbf{J}_{s,2\omega}$ to the edge-basis expansion before the calculation of Eq. (13).

The surface conductivity and the second-order surface susceptibility $\chi^{(2)}$ of the TMDC monolayer can be found in [39], where the WS₂ material is adopted in our calculation. The dimension of the TMDC monolayer is $2 \times 2 \mu\text{m}^2$ under the plane-wave illumination with a wavelength of 800 nm. Then we apply Eq. (2) to obtain the E field at the second-harmonic frequency. By rotating the monolayer and keeping the incident wave polarized along the x direction, the far-field second-harmonic intensities as a function of ϕ are calculated for both the parallel component and the perpendicular component (here we choose the analyzer $\hat{\mathbf{e}}_{2\omega}$ to be the same as $\hat{\mathbf{e}}_\omega$, i.e., the x direction). Equations (3) and (4) result in the intensities of the parallel part $I_{\parallel,2\omega} \propto \cos^2(3\phi)$ and the perpendicular part $I_{\perp,2\omega} \propto \sin^2(3\phi)$. Figures 1(b) and 1(c) show the results calculated by the EFIE solver, which are in consistency with the analytical expressions and the experimental data as well [42], validating the accuracy of the model.

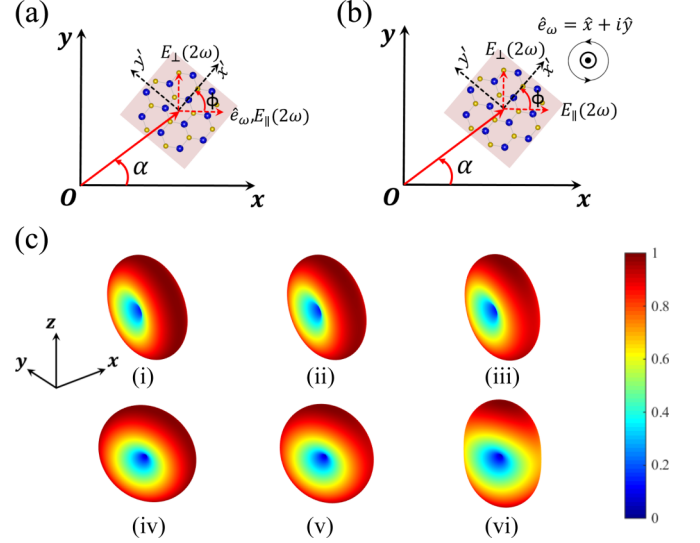


FIG. 2. (a) and (b) Rotated single TMDC flake with the local coordinates of (x', y') , where x' is the armchair direction. (a) Incident plane wave has a fixed polarization along the x axis. (b) Incident plane wave is left-circularly polarized. (c) Normalized radiation pattern of a single TMDC flake rotating 10° to achieve polarization pointing to the direction of 30° at second harmonics. The incident fundamental pump is an x -polarized plane wave propagating along the $-z$ direction. (i)–(iii) correspond to side lengths of 35 nm (0.044λ), 70 nm (0.088λ), and 140 nm (0.175λ) at fundamental frequency with wavelength λ of 800 nm; (iv)–(vi) correspond to the side lengths of 35, 70, and 140 nm at second-harmonic frequency. The color bar indicates the intensity of the normalized radiation pattern.

C. Generation of radially and azimuthally polarized beams

Figure 2(a) sets the global coordinate system as (x, y) and (x', y') as the local coordinate system of the TMDC flake, where x' is the armchair direction. The center of the square flake is placed at the position where the polar angle is α , and the polarization angle between x' and x is ϕ . According to the theory discussed above and coordinate transformation, the nonlinear conversion relation between the second-harmonic electric field and the incident fundamental E field can be linked by a Jones matrix (provided in Appendix B), i.e.,

$$\begin{bmatrix} E_{x,2\omega} \\ E_{y,2\omega} \end{bmatrix} = C\chi^{(2)} \cdot \bar{\mathbf{R}} \cdot \begin{bmatrix} E_{x,\omega} E_{x,\omega} \\ E_{x,\omega} E_{y,\omega} \\ E_{y,\omega} E_{y,\omega} \end{bmatrix}, \quad (14)$$

with

$$\bar{\mathbf{R}} = \begin{bmatrix} \cos(3\phi) & 2\sin(3\phi) & -\cos(3\phi) \\ \sin(3\phi) & -2\cos(3\phi) & -\sin(3\phi) \end{bmatrix}, \quad (15)$$

where 3ϕ is a geometric phaselike or Pancharatnam-Berry phaselike factor [47,48] due to the anisotropic nonlinearity of the TMDC material showing threefold rotational symmetry for its crystalline structure. Assume the incident wave is polarized along the x direction, i.e., $E_{y,\omega} = 0$, and let $E_{x,\omega} = 1$; then the parallel component of the SHG is $E_{\parallel,2\omega} = E_{x,2\omega} = \cos(3\phi)$, and the perpendicular component is $E_{\perp,2\omega} = E_{y,2\omega} = \sin(3\phi)$. Therefore, the resultant polarization will

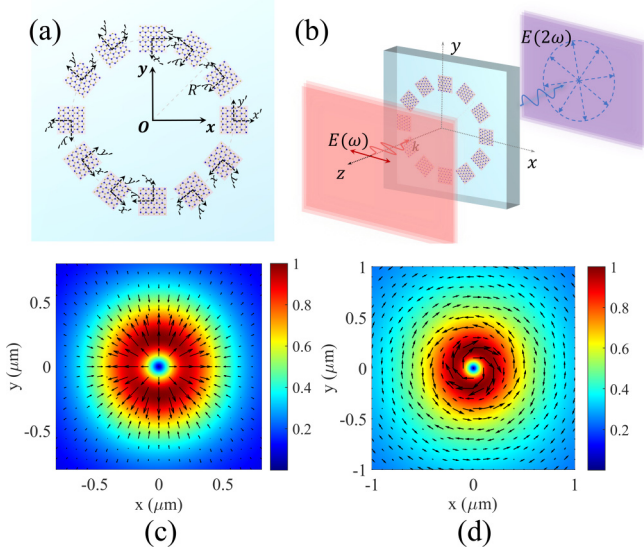


FIG. 3. (a) Design of a TMDC metasurface for generating the radially polarized beam (top view). (b) Schematic illustration of a TMDC metasurface for generating the radially polarized beam. (c) Second-harmonic E field of the radially polarized beam at the plane of $z = -400$ nm. (d) Second-harmonic E field of the azimuthally polarized beam at the plane of $z = -200$ nm. In (c) and (d), the color bar and arrows indicate the normalized intensity and the direction of polarization for the electric field on the plane, respectively.

point to the radial direction in the global system if

$$\tan(\alpha) = \frac{E_{y,2\omega}}{E_{x,2\omega}} = \tan(3\phi). \quad (16)$$

Figure 2(c) shows the normalized radiation pattern of a single TMDC flake rotating 10° to achieve the polarization pointing to 30° at the second-harmonic frequency for three side lengths of the flake under the normal-incidence plane wave polarized along the x axis at fundamental frequency. It can be found that in the subwavelength regime, the flake can be regarded as a dipole both at the fundamental frequency and at the second-harmonic frequency, with polarization pointing to the x axis and 30° , respectively. Increasing the size of the flake will be advantageous since it will increase the intensity of generated fields. However, if the dimension of the flake is too large, the radiation pattern at second harmonics will not be a dipole anymore [Fig. 2(c), diagram (vi)]. In the following discussion, the side length of the flake as a meta-atom is set as 35 nm to demonstrate the design approach.

In order to achieve the radial polarization, which is cylindrically symmetric, each square flake is centered on a circle's circumference. Figures 3(a) and 3(b) illustrate a schematic pattern of the proposed metasurface. It is important to make lateral dimensions of the flake smaller than the wavelength to suppress high-order diffraction (only specular reflection is allowed). The wavelength of incident E field is 800 nm, and the radius R of the circle is 100 nm. The meta-atoms are placed at the cylindrical coordinates of $(R, 2\pi n/N)$, where $n = 0, 1, \dots, N-1$ and $N = 12$. The corresponding angles of rotation for each flake should be $2\pi n/(3N)$ from Eq. (16). However, this orientation configuration results in

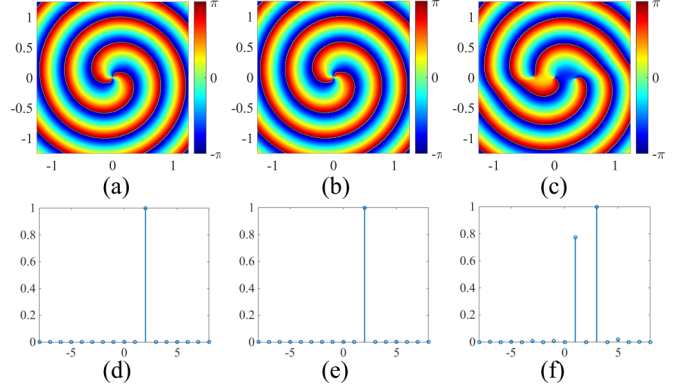


FIG. 4. Phase distributions of the second-harmonic E_ρ component for the OAM modes of (a) $l = 1$, (b) $l = 2$, and (c) $l = 3$. Fourier decomposition of the second-harmonic E_ρ component for the OAM modes of (d) $l = 1$, (e) $l = 2$, and (f) $l = 3$.

a wholly asymmetric metasurface structure and thus lowers the performance of the radially polarized beam generated (see Appendix B, Fig. 5). Exploring the threefold rotational symmetry of the nonlinear response, for instance, instead of rotating 10° centered at $(R, 30^\circ)$, the flake is rotated by 130° . The 120° incremental rotation does not change the polarization state of SHG. Similarly, for those flakes that break the symmetry, the rotating angle is added by $2\pi/3$ or $4\pi/3$. Figure 3(c) shows the transverse E-field distribution at the plane of $z = -400$ nm with x and y ranging from -0.8 to $0.8 \mu\text{m}$. A radially polarized beam with a polarization singularity can be clearly seen at the second-harmonic frequency.

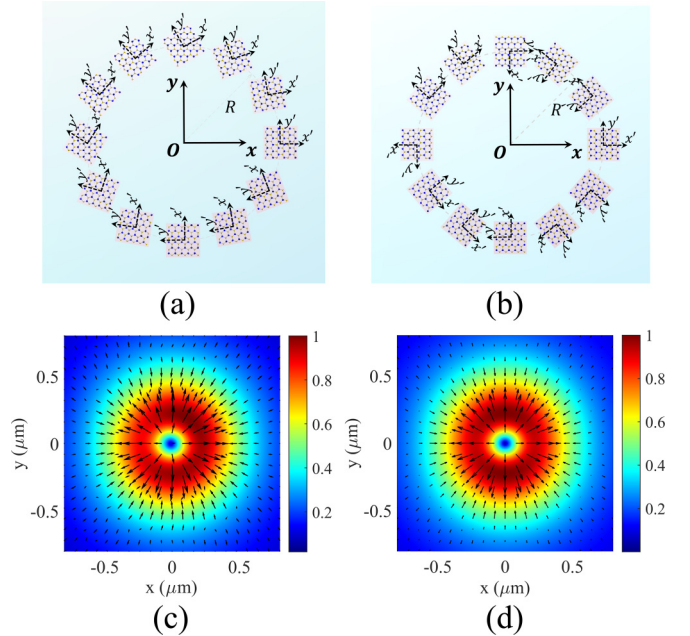


FIG. 5. (a) Schematic illustration of the metasurface with original rotating angles. (b) Schematic illustration of the metasurface with modified rotating angles. (c) Radial polarization generated by the structure in (a) on the plane of $z = -400$ nm with x and y ranging from -0.8 to $0.8 \mu\text{m}$. (d) Radial polarization generated by the structure in (b) on the same plane described in (c).

Figure 3(d) shows the azimuthally polarized beam generated at second harmonics by rotating each flake by $(2\pi n/N + \pi/2)/3$. In the same fashion, the rotating angle is adjusted by adding $2\pi/3$ or $4\pi/3$ when needed (see Appendix B). One can see the vortexlike polarization structure with a singularity at the beam center (the E field is plotted on the plane of $z = -200$ nm with x and y ranging from -1.0 to 1.0 μm).

D. Generation of orbital angular momentum

As shown in Fig. 2(b), when the vertically incident plane wave with the left-circular polarization (LCP) illuminates the flake, the radial component at second harmonics has the following form (provided in Appendix C):

$$E_{\rho,2\omega} = C\chi^{(2)}e^{i3\phi-i\alpha} = C\chi^{(2)}e^{il\alpha}, \quad (17)$$

where l is the topological charge of the OAM beam to be generated and the constants related to the incident intensity and surface susceptibilities of the TMDC flake are omitted here. The nonlinear spin-orbital interaction can be seen from the supposition of the geometric phase factors, originating from the relation between the circular polarization and rotations of two coordinate frames of (x', y') and (x, y) , which are equivalent to the translations and orientations of the anisotropically nonlinear meta-atoms. We choose to focus on E_{ρ} because $\{e^{il\alpha}\}$ is the set of eigenstates for the Helmholtz equation in the cylindrical coordinates.

From Eq. (17), the rotating angle of each flake is $\phi = (l + 1)\alpha/3$, where $\alpha = 2\pi n/N$, $n = 0, 1, \dots, N - 1$ and $N = 12$. To achieve the $l = 1$ mode, $\phi = 2\alpha/3$; for $l = 2$, $\phi = \alpha$, and for $l = 3$, $\phi = 4\alpha/3$. The threefold rotational symmetry is also explored here to modify the design. Figures 4(a)–4(c) show the phase distributions for the OAM modes with $l = 1, 2, 3$ on a plane of $z = -200$ nm (x and y range from -1.25 to 1.25 μm), with the corresponding Fourier decompositions depicted in Figs. 4(d)–4(f), respectively. When the topological charge $l = 1, 2$, the desired vortex mode is dominant, and the purity of the vortex beam is high. However, regarding the case of $l = 3$, the amplitude of the $l = 1$ mode is comparable to that of the $l = 3$ mode. The emergence of the $l = 1$ mode is due to the mutual coupling between each flake and the rotating angle $2\pi n/9$, which is double $\pi n/9$, the rotating angle for $l = 1$. For higher-order OAM modes with $l > 3$, the mutual coupling and the threefold rotational symmetry of the TMDC crystals give rise to more quasidegenerate modes.

III. CONCLUSION

In conclusion, the proposed TMDC metasurface converts fundamental plane waves to versatile structured light at second-harmonic frequencies. The generated structured light includes radially and azimuthally polarized beams (by linearly polarized plane waves) and vortex beams carrying different orders of OAM modes (by circularly polarized plane waves). The anisotropically nonlinear susceptibility with a threefold rotation-symmetrical crystalline structure makes the TMDC meta-atoms more flexible in the control of spatial structures of light at short wavelengths, which extends the spectral bandwidth of operations in optical communication or other light manipulation. The translations and orientations of each

anisotropically nonlinear meta-atom produce a geometric phase at the second harmonics, which can be understood as a characterizer of nonlinear spin-orbital interaction. Moreover, the monolayer and multilayered TMDCs can both be patterned on flat and curved substrates and be on chip integrated with other plasmonic and photonic nanostructures, which have a bright outlook in applications for next-generation optical and optoelectronic devices.

ACKNOWLEDGMENTS

This work was supported by NSF ECCS Grant No. 1609195, a Marie Skłodowska-Curie Individual Fellowship (MSCA-IFEF-ST 752898), the National Natural Science Foundation of China (Grants No. 61975177, No. 61701424, and No. 61701423), the UIUC Center for Advance Study, and the Purdue University startup package.

APPENDIX A: THREEFOLD ROTATIONAL SYMMETRY OF SHG

In this Appendix, we provide the derivation of the threefold rotational symmetry of the second-harmonic generation for the TMDC monolayer. The TMDC monolayer flake is illuminated by a normal-incidence plane wave propagating along the $-z$ direction with a linear polarization vector \hat{e}_{ω} , as shown in Fig. 1(a). The \hat{e}_{ω} can be decomposed to $E_{x,\omega} = \cos(\phi)$ and $E_{y,\omega} = \sin(\phi)$, where ϕ is the angle between the incident wave polarization and the x axis. According to Eqs. (1) and (2), the components along x and y can be expressed as

$$\begin{aligned} E_{x,2\omega} &= C\chi_{xxx}^{(2)}\cos(\phi)\cos(\phi) + C\chi_{xyy}^{(2)}\sin(\phi)\sin(\phi) \\ &= C\chi^{(2)}[\cos^2(\phi) - \sin^2(\phi)] \end{aligned} \quad (A1)$$

and

$$\begin{aligned} E_{y,2\omega} &= C\chi_{yyx}^{(2)}\sin(\phi)\cos(\phi) + C\chi_{yxy}^{(2)}\cos(\phi)\sin(\phi) \\ &= -2C\chi^{(2)}\sin(\phi)\cos(\phi). \end{aligned} \quad (A2)$$

If we choose the analyzer $\hat{e}_{2\omega}$ pointing to the fundamental polarization vector, then the component parallel to the analyzer at the second-harmonic frequency is

$$\begin{aligned} E_{\parallel}(2\omega) &= E_{x,2\omega}\cos(\phi) + E_{y,2\omega}\sin(\phi) \\ &= C\chi^{(2)}[\cos^3(\phi) - \sin^2(\phi)\cos(\phi) \\ &\quad - 2\sin(\phi)\cos(\phi)\sin(\phi)] = C\chi^{(2)}\cos(3\phi). \end{aligned} \quad (A3)$$

In the same fashion, the perpendicular component can be derived as

$$E_{\perp}(2\omega) = -E_{x,2\omega}\sin(\phi) + E_{y,2\omega}\cos(\phi) = -C\chi^{(2)}\sin(3\phi). \quad (A4)$$

APPENDIX B: DERIVATION FOR RADIAL AND AZIMUTHAL POLARIZATION

In this Appendix, we present the derivation for the Jones matrix in Eq. (14). As shown in Fig. 2(a), the global coordinate system is (x, y) , while the local system is (x', y') . The center of the TMDC flake is positioned at the polar angle α , and the angle between x' and x is ϕ . Assuming $E_{x,\omega}$ and $E_{y,\omega}$ are the

TABLE I. Rotating angles for radial polarization.

α	0°	30°	60°	90°	120°	150°	180°	210°	240°	270°	300°	330°
ϕ	0°	10°	20°	30°	40°	50°	60°	70°	80°	90°	100°	110°
ϕ'	0°	130°	140°	270°	40°	50°	180°	310°	320°	90°	220°	230°

two components of the incident wave at the fundamental frequency, then $E_{x',\omega} = E_{x,\omega} \cos(\phi) + E_{y,\omega} \sin(\phi)$, and $E_{y',\omega} = -E_{x,\omega} \sin(\phi) + E_{y,\omega} \cos(\phi)$. According to Eqs. (1) and (2), $E_{x',2\omega}$ and $E_{y',2\omega}$ can be expressed as

$$E_{x',2\omega} = C\chi^{(2)}\{[\cos^2(\phi) - \sin^2(\phi)]E_{x,\omega}E_{x,\omega} + 4\sin(\phi)\cos(\phi)E_{x,\omega}E_{y,\omega} + [\sin^2(\phi) - \cos^2(\phi)]E_{y,\omega}E_{y,\omega}\} \quad (\text{B1})$$

and

$$E_{y',2\omega} = C\chi^{(2)}\{2\sin(\phi)\cos(\phi)E_{x,\omega}E_{x,\omega} + 2[\sin^2(\phi) - \cos^2(\phi)]E_{x,\omega}E_{y,\omega} - 2\sin(\phi)\cos(\phi)E_{y,\omega}E_{y,\omega}\}. \quad (\text{B2})$$

By vector decomposition, $E_{x,2\omega}$ and $E_{y,2\omega}$ in the global system can be derived as

$$E_{x,2\omega} = E_{x',2\omega} \cos(\phi) - E_{y',2\omega} \sin(\phi) = C\chi^{(2)}[\cos(3\phi)E_{x,\omega}E_{x,\omega} + 2\sin(3\phi)E_{x,\omega}E_{y,\omega} - \cos(3\phi)E_{y,\omega}E_{y,\omega}] \quad (\text{B3})$$

and

$$E_{y,2\omega} = E_{x',2\omega} \sin(\phi) + E_{y',2\omega} \cos(\phi) = C\chi^{(2)}[\sin(3\phi)E_{x,\omega}E_{x,\omega} - 2\cos(3\phi)E_{x,\omega}E_{y,\omega} - \sin(3\phi)E_{y,\omega}E_{y,\omega}]. \quad (\text{B4})$$

Equation (14) gives a compact form for the nonlinear conversion relation.

As mentioned in Sec. II C, the original configuration of the orientation results in a wholly asymmetric metasurface structure [see Fig. 5(a)] and thus affects the performance of the radial polarization, as shown in Fig. 5(c). Figures 5(b) and 5(d) show the modified design and the generated radial polarization.

The polar angle α , rotating angle ϕ , and modified rotating angle ϕ' for radial polarization and azimuthal polarization are given in Tables I and II, respectively.

APPENDIX C: DERIVATION FOR ORBITAL ANGULAR MOMENTUM

In this Appendix, we provide the derivation in the generation of the orbital angular momentum. The left-circular

TABLE II. Rotating angles for azimuthal polarization.

α	0°	30°	60°	90°	120°	150°	180°	210°	240°	270°	300°	330°
ϕ	30°	40°	50°	60°	70°	80°	90°	100°	110°	120°	130°	140°
ϕ'	150°	40°	50°	180°	310°	320°	90°	220°	230°	0°	130°	140°

polarization (LCP) is normalized as

$$|\mathbf{L}\rangle = \frac{1}{\sqrt{2}} \begin{pmatrix} 1 \\ i \end{pmatrix}. \quad (\text{C1})$$

With the LCP illumination, the electric field along x' and y' at the fundamental frequency can be expressed as

$$E_{x',\omega} = \frac{1}{\sqrt{2}}[\cos(\phi) + i\sin(\phi)] = \frac{1}{\sqrt{2}}e^{i\phi} \quad (\text{C2})$$

and

$$E_{y',\omega} = \frac{1}{\sqrt{2}}[-\sin(\phi) + i\cos(\phi)] = \frac{i}{\sqrt{2}}e^{i\phi}. \quad (\text{C3})$$

Then the second-harmonic components along x' and y' are obtained by Eqs. (1) and (2) (here the parameters $C\chi^{(2)}$ are omitted):

$$E_{x',2\omega} = \frac{1}{2}e^{i2\phi} - \frac{-1}{2}e^{i2\phi} = e^{i2\phi} \quad (\text{C4})$$

and

$$E_{y',2\omega} = -\frac{i}{2}e^{i2\phi} + \frac{-i}{2}e^{i2\phi} = -ie^{i2\phi}. \quad (\text{C5})$$

Returning to the global system, $E_{x,2\omega}$ and $E_{y,2\omega}$ have the following expressions:

$$E_{x,2\omega} = E_{x',2\omega} \cos(\phi) - E_{y',2\omega} \sin(\phi) = e^{i2\phi} \cos(\phi) + ie^{i2\phi} \sin(\phi) = e^{i3\phi} \quad (\text{C6})$$

and

$$E_{y,2\omega} = E_{x',2\omega} \sin(\phi) + E_{y',2\omega} \cos(\phi) = e^{i2\phi} \sin(\phi) - ie^{i2\phi} \cos(\phi) = -ie^{i3\phi}. \quad (\text{C7})$$

As mentioned in Sec. II D, E_ρ is chosen to demonstrate the generation of orbital angular momentum since $e^{i\ell\alpha}$ is the set of eigenstates for the Helmholtz equation in the cylindrical coordinates. For a flake centered with polar angle α , $E_{\rho,2\omega}$ is expressed as

$$E_{\rho,2\omega} = E_{x,2\omega} \cos(\alpha) + E_{y,2\omega} \sin(\alpha) = e^{i3\phi} \cos(\alpha) - ie^{i3\phi} \sin(\alpha) = e^{i3\phi - i\alpha}. \quad (\text{C8})$$

By choosing the proper ϕ , the relation $e^{i\ell\alpha} = e^{i3\phi - i\alpha}$ can be established, which indicates the interactions between spin angular momentum at the fundamental frequency and orbital angular momentum at the second-harmonic frequency.

- [1] F. Cardano and L. Marrucci, *Nat. Photonics* **9**, 776 (2015).
- [2] S. Restuccia, D. Giovannini, G. Gibson, and M. Padgett, *Opt. Express* **24**, 27127 (2016).
- [3] L. Zhu and J. Wang, *Opt. Lett.* **40**, 5463 (2015).
- [4] M. J. Padgett, *Opt. Express* **25**, 11265 (2017).
- [5] Q. Zhan, *Adv. Opt. Photonics* **1**, 1 (2009).
- [6] Y.-Q. Zhang, X.-Y. Zeng, R.-R. Zhang, Z.-J. Zhan, X. Li, L. Ma, C.-X. Liu, C.-W. He, and C.-F. Cheng, *Opt. Lett.* **43**, 4208 (2018).
- [7] K. Y. Bliokh, F. Rodríguez-Fortuño, F. Nori, and A. V. Zayats, *Nat. Photonics* **9**, 796 (2015).
- [8] X. Xie, Y. Chen, K. Yang, and J. Zhou, *Phys. Rev. Lett.* **113**, 263901 (2014).
- [9] C. Min, Z. Shen, J. Shen, Y. Zhang, H. Fang, G. Yuan, L. Du, S. Zhu, T. Lei, and X. Yuan, *Nat. Commun.* **4**, 2891 (2013).
- [10] M. D. Lew and W. Moerner, *Nano Lett.* **14**, 6407 (2014).
- [11] L. Carretero, P. Acebal, C. Garcia, and S. Blaya, *IEEE Photonics J.* **7**, 1 (2015).
- [12] N. Bozinovic, Y. Yue, Y. Ren, M. Tur, P. Kristensen, H. Huang, A. E. Willner, and S. Ramachandran, *Science* **340**, 1545 (2013).
- [13] H. Rubinsztein-Dunlop, A. Forbes, M. V. Berry, M. R. Dennis, D. L. Andrews, M. Mansuripur, C. Denz, C. Alpmann, P. Banzer, and T. Bauer, *J. Opt.* **19**, 013001 (2016).
- [14] D. Pohl, *Appl. Phys. Lett.* **20**, 266 (1972).
- [15] Y. Kozawa and S. Sato, *Opt. Lett.* **30**, 3063 (2005).
- [16] M. A. Ahmed, A. Voss, M. M. Vogel, and T. Graf, *Opt. Lett.* **32**, 3272 (2007).
- [17] T. Hirayama, Y. Kozawa, T. Nakamura, and S. Sato, *Opt. Express* **14**, 12839 (2006).
- [18] T. Su, R. P. Scott, S. S. Djordjevic, N. K. Fontaine, D. J. Geisler, X. Cai, and S. Yoo, *Opt. Express* **20**, 9396 (2012).
- [19] P. Yu, S. Chen, J. Li, H. Cheng, Z. Li, W. Liu, B. Xie, Z. Liu, and J. Tian, *Opt. Lett.* **40**, 3229 (2015).
- [20] A. Arbabi, Y. Horie, M. Bagheri, and A. Faraon, *Nat. Nanotechnol.* **10**, 937 (2015).
- [21] Y. He, G. Guo, T. Feng, Y. Xu, and A. E. Miroshnichenko, *Phys. Rev. B* **98**, 161112(R) (2018).
- [22] W. Buono, L. Moraes, J. Huguenin, C. Souza, and A. Khoury, *New J. Phys.* **16**, 093041 (2014).
- [23] G. Gariepy, J. Leach, K. T. Kim, T. J. Hammond, E. Frumker, R. W. Boyd, and P. B. Corkum, *Phys. Rev. Lett.* **113**, 153901 (2014).
- [24] A. Fleischer, O. Kfir, T. Diskin, P. Sidorenko, and O. Cohen, *Nat. Photonics* **8**, 543 (2014).
- [25] A. E. Minovich, A. E. Miroshnichenko, A. Y. Bykov, T. V. Murzina, D. N. Neshev, and Y. S. Kivshar, *Laser Photonics Rev.* **9**, 195 (2015).
- [26] W. Ye, F. Zeuner, X. Li, B. Reineke, S. He, C.-W. Qiu, J. Liu, Y. Wang, S. Zhang, and T. Zentgraf, *Nat. Commun.* **7**, 11930 (2016).
- [27] G. Li, S. Zhang, and T. Zentgraf, *Nat. Rev. Mater.* **2**, 17010 (2017).
- [28] P. Chen, S.-J. Ge, W. Duan, B.-Y. Wei, G.-X. Cui, W. Hu, and Y.-Q. Lu, *ACS Photonics* **4**, 1333 (2017).
- [29] W. Luo, S. Sun, H.-X. Xu, Q. He, and L. Zhou, *Phys. Rev. Appl.* **7**, 044033 (2017).
- [30] X. Ling, X. Zhou, K. Huang, Y. Liu, C.-W. Qiu, H. Luo, and S. Wen, *Rep. Prog. Phys.* **80**, 066401 (2017).
- [31] X. Y. Z. Xiong, A. Al-Jarro, L. J. Jiang, N. C. Panoiu, and W. E. I. Sha, *Phys. Rev. B* **95**, 165432 (2017).
- [32] G. Li, L. Wu, K. F. Li, S. Chen, C. Schlickriede, Z. Xu, S. Huang, W. Li, Y. Liu, E. Y. Pun, T. Zentgraf, K. W. Cheah, Y. Luo, and S. Zhang, *Nano Lett.* **17**, 7974 (2017).
- [33] S. Keren-Zur, L. Michaeli, H. Suchowski, and T. Ellenbogen, *Adv. Opt. Photonics* **10**, 309 (2018).
- [34] H.-X. Xu, G. Hu, Y. Li, L. Han, J. Zhao, Y. Sun, F. Yuan, G.-M. Wang, Z. H. Jiang, X. Ling, T. J. Cui, and C.-W. Qiu, *Light: Sci. Appl.* **8**, 3 (2019).
- [35] P. Li, I. Dolado, F. J. Alfaro-Mozaz, F. Casanova, L. E. Hueso, S. Liu, J. H. Edgar, A. Y. Nikitin, S. Vélez, and R. Hillenbrand, *Science* **359**, 892 (2018).
- [36] C.-H. Liu, J. Zheng, S. Colburn, T. K. Fryett, Y. Chen, X. Xu, and A. Majumdar, *Nano Lett.* **18**, 6961 (2018).
- [37] X. Hong, G. Hu, W. Zhao, K. Wang, S. Sun, R. Zhu, J. Wu, W. Liu, K. P. Loh, A. T. S. Wee, B. Wang, A. Alù, C.-W. Qiu, and P. Lu, *Research* **2020**, 9085782 (2020).
- [38] F. Spreyer, R. Zhao, L. Huang, and T. Zentgraf, *Nanophotonics* **9**, 351 (2020).
- [39] M. Weismann and N. C. Panoiu, *Phys. Rev. B* **94**, 035435 (2016).
- [40] S. Yang, D. C. Liu, Z. L. Tan, K. Liu, Z. H. Zhu, and S. Q. Qin, *ACS Photonics* **5**, 342 (2018).
- [41] M.-H. Chiu, H.-L. Tang, C.-C. Tseng, Y. Han, A. Aljarb, J.-K. Huang, Y. Wan, J.-H. Fu, X. Zhang, W.-H. Chang, D. A. Muller, T. Takenobu, V. Tung, and L.-J. Li, *Adv. Mater.* **31**, 1900861 (2019).
- [42] L. M. Malard, T. V. Alencar, A. P. M. Barboza, K. F. Mak, and A. M. de Paula, *Phys. Rev. B* **87**, 201401(R) (2013).
- [43] H. Zeng, G.-B. Liu, J. Dai, Y. Yan, B. Zhu, R. He, L. Xie, S. Xu, X. Chen, W. Yao, and X. Cui, *Sci. Rep.* **3**, 1608 (2013).
- [44] W. C. Chew, M. S. Tong, and B. Hu, *Synth. Lect. Comput. Electromagn.* **3**, 241 (2008).
- [45] L. L. Meng, X. Y. Xiong, T. Xia, and L. J. Jiang, *IEEE Antennas Wireless Propag. Lett.* **16**, 1655 (2017).
- [46] M. C. Lucking, K. Beach, and H. Terrones, *Sci. Rep.* **8**, 10118 (2018).
- [47] Z. Bomzon, G. Biener, V. Kleiner, and E. Hasman, *Opt. Lett.* **27**, 1141 (2002).
- [48] M. L. Chen, L. J. Jiang, and W. E. Sha, *J. Appl. Phys.* **119**, 064506 (2016).